Chemical Engineering Journal 437 (2022) 135163

Contents lists available at ScienceDirect

Chemical Engineering Journal

journal homepage: www.elsevier.com/locate/cej

Development of polyacrylonitrile/perovskite catalytic membrane with abundant channel-assisted reaction sites for organic pollutant removal

Longfei Zhang [1], Na Yang [1], Yuhang Han, Xiang Wang, Shulin Liu, Luhong Zhang, Yongli Sun, Bin Jiang [*]

ARTICLE INFO

Keywords:
Perovskite
Catalytic membrane
Peroxymonosulfate
Degradation

ABSTRACT

Catalytic membrane that can simultaneously enable physical separation and advanced oxidation process is considered as a novel approach for wastewater remediation; however, the unsatisfied catalytic performance and instability impede its further application. In this study, Fe doped $LaCoO_3$ perovskite with tunable electron structure was employed as a heterogeneous catalyst and incorporated with Polyacrylonitrile ultrafiltration membrane via a controlled phase inversion method. Owing to the continuous outflow of the intermediates and enriched concentration gradients in membrane channels, the catalytic membrane exhibited exceptional catalytic performance and stability under cross-flow apparatus. Correspondingly, over 99% of tetracycline hydrochloride can be degraded via activating peroxymonosulfate in 36 min under the flux of 220 L/m^2h. Besides, the catalytic membrane with suitable pore size could exclude natural organic matter and selectively assist the degradation of pollutants in membrane channels due to a massive generation of sulfate radicals and singlet oxygen (equivalent to a retention time of 1.64 s). Following this, the degradation pathways and toxicity analysis of the intermediates were investigated to further verify the catalysis mechanism and the reduced toxicity of treated solution. Overall, it can be concluded that the integration of membrane and catalytic oxidation is effective for enhancing wastewater purification efficiency.

1. Introduction

With the rapid development of industrialization and population growth, water scarcity has dramatically deteriorated [1]. Tetracycline hydrochloride (TC), a typical therapeutic medicine, has been widely used in animal growth. Inevitably, TC tends to be discharged into the aquatic ecosystem owing to its poor biodegradability, thereby posing a potential threat to the human health [1,2]. Sulfate radical-based advanced oxidation processes (SR-AOPs) have been considered as a prominent strategy to eliminate refractory contaminants, which accounts for the high catalytic efficiency, selectivity, and a wide pH range [3–5]. Various heterogeneous catalysts (transition metal oxides, alloys, carbon-based materials, etc.) have been developed to activate peroxymonosulfate (PMS) [6–8]. Through the scission of peroxo-bond, sulfate radicals can be generated and then react with organic compounds via electron transfer, realizing oxidation or partial mineralization of organic pollutants [9]. However, heterogeneous catalysts tend to agglomerate during the reaction, which restricts the reaction of PMS and pollutants on the catalyst sites and thus impedes catalytic activity consequently [10,11]. Besides, the re-utilization of powder catalysts requires additional separation processes such as filtration or centrifugation, which undoubtedly lose the active component. Furthermore, the sluggish catalytic efficiency under various external conditions, especially with the co-existence of natural organic matter (NOM), remains an imperative issue that needs to be addressed [12,13].

Integrating heterogeneous catalysts with an appropriate support having selective separation ability and high loading capacity can be considered as a highly effective approach [11,14]. Therefore, the coupling of AOPs and membrane technology has received a great deal of attention [15–17]. Catalytic membrane with a dense skin layer is capable for allowing its selectivity by physical pore sieving, while porous structure offers immobilization sites for heterogeneous catalysts, constructing micro reaction sites in tortuous membrane channels [18,19]. Unlike the batch experiment of common AOPs, catalytic membrane realizes the simultaneous separation/degradation processes in one system under external pressure [20,21]. In other words, the skin layer excludes macromolecular pollutants that are larger than pores, ensuring the efficient degradation of small organic compounds in the

* Corresponding author at: School of Chemical Engineering and Technology, Tianjin University, Tianjin 300072, PR China.
E-mail address: binj@tju.edu.cn (B. Jiang).
[1] These authors contribute equally to this work.

https://doi.org/10.1016/j.cej.2022.135163

Available online 9 February 2022

membrane channels [22]. Besides, the continuous operation of catalytic membrane reduces the residence time of intermediate products at reaction sites, which improves the catalytic efficiency and ensures the recycling capacity. Furthermore, anchoring the heterogeneous catalysts in the membrane matrix can regulate membrane structure, which is beneficial for improving hydrophilicity and permeability [23]. With dual functionalities of membrane separation and catalytic oxidation, the decontamination efficiency of the wastewater can be considerably enhanced [24].

The rational design of functional catalysts is of great importance for the construction of high performance catalytic membranes. Until now, extensive efforts have been applied to fabricate catalytic membranes with favorable separation/degradation performance. For instance, Zhang et al. incorporated FeOCl nano-catalysts into ceramic ultrafiltration membrane pore to form a membrane reactor, and it was observed that it exhibited great degradation capacity towards various organic pollutants. Besides, the membrane could exclude NOM by physical rejection, and selectively assist the catalytic oxidation of small organic matter in membrane matrix under confinement [25]. Lin et al. enchased Prussian blue in the micro-cluster of PVDF membrane, enabling instantaneous degradation of recalcitrant [18]. Zhang et al. prepared a novel MnOOH coated nylon membrane and found that the forced flow in membrane voids contributed to the increment of 2, 4-Dichlorophenol degradation [26]. However, the catalytic properties of membranes are mainly dominated by the catalysts. Therefore, fabricating functional catalysts with superior catalytic activity and stability to improve the intrinsic separation/catalytic performance of catalytic membrane is of great importance. Compared with the catalyst of single-metal sites, multi-component oxides such as spinel and perovskite oxide have demonstrated an excellent catalytic performance because of the electron transfer between the metal sites [27,28]. Perovskite oxide generally exhibits a ABO_3 structure, where A sites are dominated by the rare earth or alkaline rare earth metals while B sites mainly comprise a 3d-transition metal [29]. Owing to the fascinating catalytic activity, stability, and tunable electronic structure, cobalt-based perovskite oxides ($LaCoO_3$, $SrCoO_3$, $CoTiO_3$, etc.) have been widely reported as promising catalysts to activate PMS to realize refractory pollutant elimination [30,31]. Notably, heteroatom doping has been widely employed to tune the intrinsic catalytic performance of $LaCoO_3$, which can rationally generate oxygen vacancies and facilitate electron transfer, resulting in an enhanced catalytic activity toward PMS activation [32,33]. As an adjacent element of Co, Fe possesses a similar ionic radius and electronegativity compared with Co, which exhibits feasibility to substitute part of Co in $LaCoO_3$ structure [28]. Besides, Fe doping can facilitate the activation efficiency of PMS as an electron-donator to further promote the degradation capacity of pollutants [34]. However, current research rarely involves the combination of perovskite catalysts and membranes, and therefore the performance and mechanism of the catalytic membrane should be elucidated.

In this work, $LaCoO_3$ perovskite was synthesized via a typical sol–gel method and further tuned the catalytic activity by doping Fe on B sites. Afterward, Fe doped $LaCoO_3$ was employed as functional catalysts to integrate with polyacrylonitrile (PAN) membrane via a controllable phase inversion method. The as-prepared membrane with capacities of separation and catalytic degradation could demonstrate a promising cleaning efficiency towards the recalcitrant organic pollutants. The separation/catalytic performance of the catalytic membrane was analyzed in the presence of NOM. Besides, the mechanism and stability of the catalytic membrane were thoroughly investigated. Furthermore, the toxic analysis of the degradation intermediates was also performed.

2. Experimental section

2.1. Chemical and reagents

Citric acid and iron nitrate nonahydrate ($Fe(NO_3)_3{\cdot}9H_2O$) were obtained from Aladdin Chemical Reagent Co., Ltd (Shanghai, China). Lanthanum nitrate hexahydrate ($La(NO_3)_3{\cdot}6H_2O$), cobalt nitrate hexahydrate ($Co(NO_3)_2{\cdot}6H_2O$), ammonium hydroxide ($NH_3{\cdot}H_2O$), methanol (MeOH), *tert*-butyl alcohol (TBA), and furfural (FFA) were purchased from Guangfu Chemical Reagent Co. LTD (Tianjin, China). Peroxymonosulfate ($2KHSO_5{\cdot}KHSO_4{\cdot}K_2SO_4$), N-methylpyrrolidone (NMP), humic acid (HA), PAN powder (Mw = 150000 g/mol), and tetracycline hydrochlorid (TC) were supplied by Kermel Chemical Reagent Co. LTD (Tianjin, China). All chemicals were analytic grade and used as received.

2.2. Preparation and modification of perovskite oxides

The Fe doped $LaCoO_3$ perovskite was prepared by a sol–gel method. In a typical synthesis procedure, 0.1 mol/L $La(NO_3)_3{\cdot}6H_2O$, x mol/L $Co(NO_3)_2{\cdot}6H_2O$ (x = 0.05–0.1 mol/L), 1-x/L mol $Fe(NO_3)_3{\cdot}9H_2O$ were dissolved in 50 mL deionized water, the feed molar ratios of $Co(NO_3)_2{\cdot}6H_2O$ to $Fe(NO_3)_3{\cdot}9H_2O$ were set from 0.5:9.5 to 5:5. Afterward, 0.3 mol/L citric acid was introduced as the complex agent. The mixture was stirred and ultrasonicated for 15 min. pH of the solution was then adjusted to 9.0 by $NH_3{\cdot}H_2O$, and the color of the solution gradually darken during this process. After this, the above solution was transferred to a water bath at 80 °C to evaporate extra water and a uniform precursor was then obtained. Afterward, the precursor was dried at 100 °C overnight, following by calcination at 700 °C with a heating rate of 5 °C/min and kept for 3 h. The powder catalysts were ground and labeled as LCO ($LaCoO_3$) and LFCXY, where X is the feed doping ratios of Fe and Y represents the feed ratios of Co.

2.3. Construction of catalytic membrane

Briefly, several amounts of Fe doped $LaCoO_3$ perovskite oxides (feed molar ratio of Fe:Co = 1:9) were added to 20 mL NMP solution and dispersed by sonication for 30 min. Then, PAN powder (12 wt%) was introduced into the mixture at 60 °C and stirred for 3 h to obtain a homogeneous casting solution. After removing air bubbles in 60 °C vacuum atmosphere for 12 h, the casting solution was slowly poured on the glass plate and then scraped by a casting knife with various thicknesses. Afterward, the plate was transferred to a water bath to complete the phase inversion process and kept for another 36 h. The catalytic membrane was obtained and labeled as PAN/LFC-x in accordance with the loading amount of perovskite oxides.

2.4. Characterization

The morphologies of the perovskite and catalytic membrane were observed using scanning electron microscope (SEM, Hitachi S4800, Japan), and transmission electron microscope (TEM, JEM-F200 Japan) with energy dispersive spectrometer was applied to obtain the chemical compositions of the material and catalytic membrane. The crystal structure of the sample was characterized by X-ray diffractometer (XRD, Bruker, D8 Advance, Germany) with 2θ range of 20°-80°. The element composition of the catalyst was determined by X-ray photoelectron spectrometer (XPS, ESCALAB 250Xi, UK) before and after reaction. Electrochemical impedance spectroscopy (EIS) analysis was employed to assess the electron transfer capacity of the samples using Ag/AgCl as the reference electrode, and the counter electrode was commercial Pt electrode. The hydrophilicity of the catalytic membrane was evaluated using water contact angle as the indicator and tested by contact angle equipment (Powereach, China). The concentration of TC aqueous solution was measured by ultraviolet–visible spectroscopy (UV–vis 4802S, Unico, USA) at the wavelength of 357 nm. Besides, the mineralization rate of the feed and treated solution was verified by total organic carbon analyzer (TOC, Shimadzu, Japan). Furthermore, the intermediate products of the TC degradation were detected by High performance liquid chromatography-tandem mass spectrometry (Thermo Vanquish UHPLC-LTQ XL, USA). Electron paramagnetic resonance (EPR) analysis

was also carried out to monitor the reactive oxygen species by employing 5,5-dimethyl-1-pyrroline-N-oxide (DMPO) and 2,2,6,6-tetramethyl-4-piperidine (TEMP) as the spin-trapping agents. Inductively coupled plasma optical emission spectrometer analysis (ICP-OES, VISTA-MPX, USA) was employed to investigate the proportion of catalyst in the membrane matrix and the amount of metal ion leaching under various operating conditions.

2.5. Evaluation of catalytic and separation performance

TC was used as the target pollutant to evaluate the catalytic activities of the powder catalyst and catalytic membrane. In a typical procedure, 10 mg of powder catalyst was dispersed in a 100 mL aqueous solution with TC concentration of 20 mg/L under constant magnetic stirring, following by the addition of 1.0 mM PMS to initiate the catalytic oxidation. Periodically, the sample was withdrawn by a 0.22 μm PVDF filter, and the TC concentration was then recorded.

Cross-flow apparatus was employed to verify the separation and catalytic performance of the catalytic membrane. The permeate flux of the membrane was calculated by Eq. (1).

$$F = \frac{V}{A \times t \times P} \tag{1}$$

where F is the flux corresponding to the permeability (L/m^2h), V is the permeate volume (L), A means the effective filtration area (7.0 cm^2) and P is the operating pressure (bar).

The porosity was calculated via Eq. (2).

$$\varepsilon = \frac{W_w - W_d}{\rho_w A \delta} \tag{2}$$

where W_w and W_d are the weight of the membrane when fully wetted by water and dried after the water is completely evaporated, respectively. ρ_w represents the density of deionized water (g/cm^3), and δ means the thickness of the membrane (cm) while A is the test area of the membrane (7.0 cm^2).

The rejection of the catalytic membrane was tested by verifying the concentration of HA before and after filtration according Eq. (3).

$$R = \frac{C_o - C}{C_0} \times 100\% \tag{3}$$

where R is the rejection ratio of the HA, C_0 and C represent the initial and treated HA concentration.

The catalytic performance was also investigated under varying reaction conditions. Briefly, an amount of 500 mL with concentration of 10 mg/L TC solution was prepared and employed as the feed stream. A certain amount of PMS was introduced to trigger the degradation process. TC was degraded in membrane channels when contacting with catalyst embedded in membrane matrix under various operating pressure and finally flowed out through the membrane. The sample was withdrawn at certain time intervals, and the concentration of pollutant was evaluated accordingly. To determine the separation/catalytic performance of the membrane, simulated wastewater containing HA and TC was prepared and the separation and catalytic performance were then tested. It should be noted that the concentration of TC should be evaluated after secondary filtration by another 0.22 μm PVDF membrane. The reaction rate constant (k) was analyzed by pseudo-first-order kinetics equation as Eq. (4).

$$\ln\frac{C_t}{C_0} = -kt \tag{4}$$

where C_0 means the initial TC concentration (mg/L), C_t is the TC concentration under various sampling time t (min).

The anti-fouling performance of the membrane was performed and described in supporting information. Besides, the effects of various operating conditions (operating pressure, pH, temperature, etc.) on the membrane performance were also investigated.

3. Results and discussion

3.1. Morphology and structure of the functional catalysts

The morphologies of perovskite oxides are shown in Fig. S1-S2. As depicted in Fig. S1 (a, b), both pristine $LaCoO_3$ and Fe doped $LaCoO_3$ exhibited an evident agglomeration phenomenon, which mainly comprises the spherical structure with a particle size of about 20 nm. The introduction of Fe element demonstrated a limited effect on the morphology of the catalyst. To confirm the existence of Fe element, EDS mapping was employed and is shown in Fig. S1 (c, d), the results demonstrated that La, Co, Fe, O elements were uniformly distributed, and the relevant atomic ratio was 20.13%, 23.25%, 1.96%, and 54.67%, respectively, which is similar to the feed molar ratio (Fig. S2). TEM images of Fe doped $LaCoO_3$ perovskite are shown in Fig. 1. Consistent with the SEM morphology, the particles were agglomerated (Fig. 1(a)). HR-TEM image shown in Fig. 1(b) exhibited the lattice fringe spacing of 0.383 nm, corresponding to (1 1 0) crystal planes of the Fe doped $LaCoO_3$ perovskite. Besides, Fig. 1(c, d) confirmed the uniform distribution of the elements. XRD patterns of the pristine and Fe doped $LaCoO_3$ perovskite oxides are depicted in Fig. 2(a). The $LaCoO_3$ exhibited the typical crystal structure of perovskite, the feature peaks centered at 23.3°, 32.9°, 40.7°, 47.5°, 58.9°, and 68.9°, which corresponds to (1 1 0), (−1 1 0), (0 2 0), (1 2 0), (1 3 0), and (−2 2 0) planes, respectively [35]. Besides, when increasing Fe content, no crystal structures of other metal oxides were found. Furthermore, the diffraction peaks shifted to lower angles, and the absence of the doublet peaks at 32.9° and 58.9° was found at higher Fe doping content. This observance indicates an increased unit cell parameters according to the enlarged ionic radius of Fe^{3+} ((0.64 Å) to Co^{3+} (0.63 Å), and further confirms that Fe element was successfully introduced into $LaCoO_3$ crystal structure to replace part of Co [28]. The changing in the crystal parameters after Fe doping is further investigated through the Rietveld refinement shown in Table S1. A growing lattice size was confirmed when Fe was doped in $LaCoO_3$ structure. However, the crystal structure changed from hexagonal to orthorhombic as Fe doping ratio further increased to 5:5. The shrink of the crystal size is ascribed to the principle of electrical neutrality, which ensures structural stability by changing crystal structure. The catalytic performance of Fe doped $LaCoO_3$ was evaluated. As shown in Fig. S3 (a), PMS alone exhibited restricted degradability to TC, and only 23% of TC was eliminated within 30 min. Besides, the adsorption capacity of the catalyst was restricted because of the low specific surface area (5.11 m^2/g) (Fig. S4). However, in the presence of $LaCoO_3$, the catalytic performance improved dramatically. 92.2% of TC can be degraded within 30 min. Furthermore, Fe doping can further enhance catalytic performance when doping ratio ranges from 0.5:9.5 to 2:8. Whereas, the degradation ability was interfered with a further increase of Fe doping ratio. This can be related to the reduction of Co content, which is regarded as the most effective activating element in PMS induced catalytic oxidation processes. Correspondingly, the relative reaction k constant was determined and shown in Fig. S3(b), the k value was 0.1187, 0.1681, 0.1871, 0.1690, 0.08574, 0.04649, 0.03186 min^{-1} for $LaCoO_3$ and Fe doped $LaCoO_3$ with various doping ratios (from 0.5:9.5 to 5:5), respectively. Therefore, LFC19 was employed as the functional catalyst to fabricate catalytic membrane to further improve water purification capacity. XPS analysis was employed to explore the surface element content and valence state of the catalysts. Signals of La, Fe, Co, and O were detected in the survey of LFC19 (Fig. S5). Identifying as the most crucial role to activate PMS, the valence state of Co element was analyzed and shown in Fig. 2(b). The high-resolution peaks of Co were divided into Co $2p_{3/2}$ (~779.6 eV) and Co $2p_{1/2}$ (~794.7 eV) spin–orbit lines. The fitted peaks located at ~ 778.8 and ~ 794.6 eV represented Co(III) while the peaks centered at ~ 796.8 and 781.1 eV can be ascribed as Co(II) [36]. The

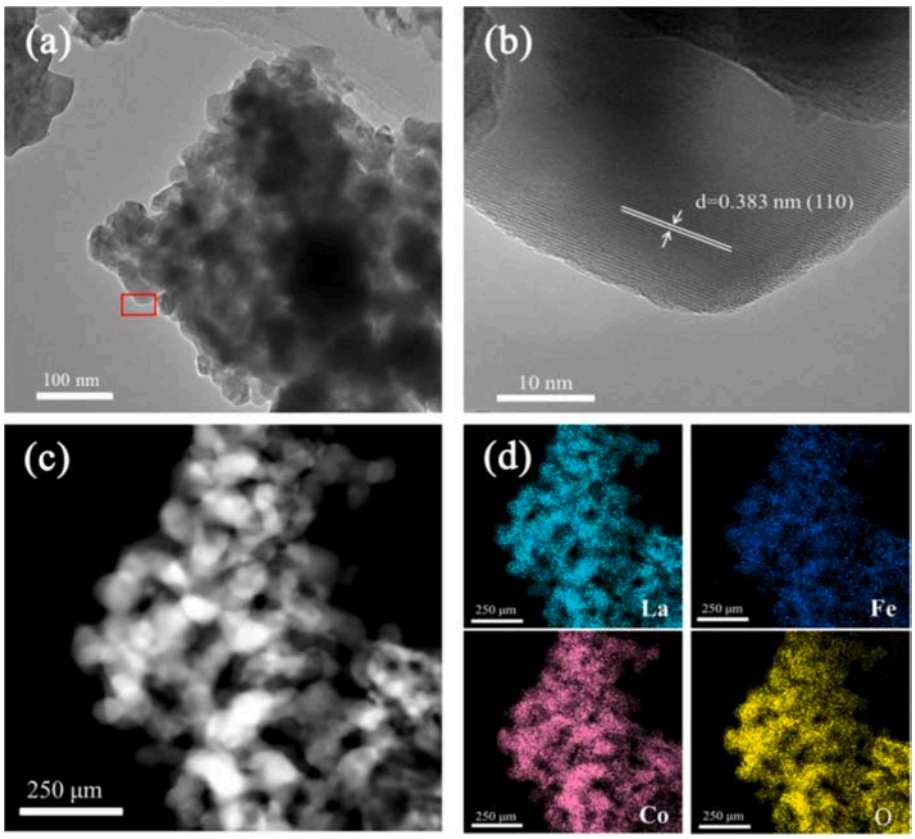

Fig. 1. TEM morphology of LFC19 (a, b) and EDS mapping of the catalyst (c, d).

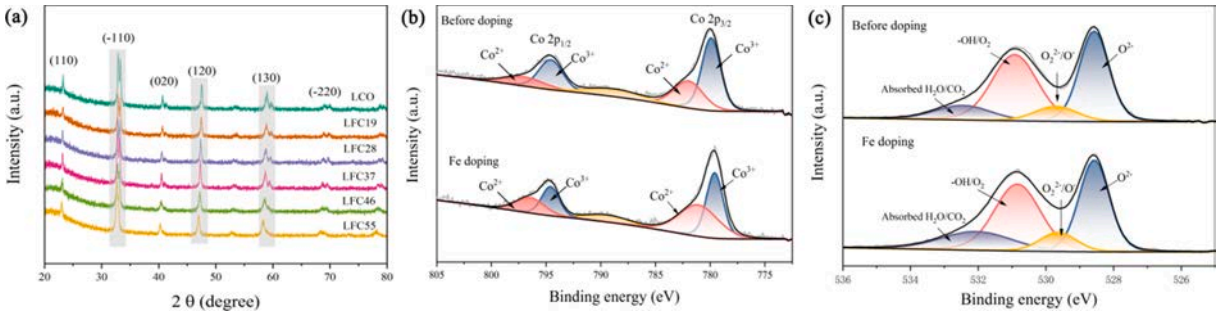

Fig. 2. XRD patterns of the perovskite $LaCoO_3$ and $LaCoO_3$ with various Fe doping ratios (a), XPS analysis of Co 2p spectrum (b), and O 1 s spectrum (c).

overall ratio of the Co^{II}/Co^{III} increased from 0.73 to 1.04 when 10% Fe was introduced into $LaCoO_3$ structure. As mentioned in previous literature, low valence of Co was more conducive to the activation of PMS. Additionally, a higher Co^{II}/Co^{III} ratio can lead to a stronger catalytic activity [33]. As manifested in Fig. 2(c), the O 1 s spectrum of perovskite can be assigned as lattice oxygen (~528.6 eV), hydroxyl groups (–OH) at ~ 530.9 eV, surface carbonate/absorbed H_2O (532.4 eV), and highly oxidative oxygen species (O_2^{2-}/O^-) at 529.6 eV [37,38]. Specifically, the appearance of O_2^{2-}/O^- can be inferred as the evidence of the presence of oxygen vacancies [39]. When Fe was doped in $LaCoO_3$ structure, the content of lattice oxygen decreased from 35.2% to 32.6%, while an increase was found in the content of –OH group from 39.4% to 42.2% and O_2^{2-}/O^- from 8.4% to 10.9%. Correspondingly, the increased –OH group strengthened the hydrophilicity of the catalyst, which resulted in an enhanced dispersity. Furthermore, the appearance of oxygen vacancies contributed to the reduction of Co valence state, and thus improves the catalytic performance. The electronic conductivity of the pristine and Fe doped $LaCoO_3$ was evaluated through EIS Nyquist plots (Fig. S6). A decreased semicircle diameter of LFC19 was observed to compare with LCO. This phenomenon showed that a lower electron transfer resistance when Fe was introduced, thereby accelerating the electron transfer between the catalyst and PMS and improving the catalytic activity.

The morphologies of the catalytic membrane are illustrated in Fig. 3. As depicted in Fig. 3(a, b), the cross-sectional morphology of PAN-based catalytic membrane presented typical finger-like pores, which provides tortuous channels for the rapid transport of the permeate solution. As more of LFC embedding in the membrane matrix, more sponge-like structures were observed together with the appearance of the microvoids in the sub-layer of the catalytic membrane. This could be attributed to the increased viscosity of the casting solution, which could prolong the progress of phase inversion and thereby increases the porosity. The tortuous channels and increased porosity of the catalytic membrane endowed more contact probability of PMS and pollutant on micro reaction sites, further accelerating the degradation of target pollutants. However, when LFC content reached 5%, the microvoids in sublayer diminished owing to the excessively high viscosity of casting

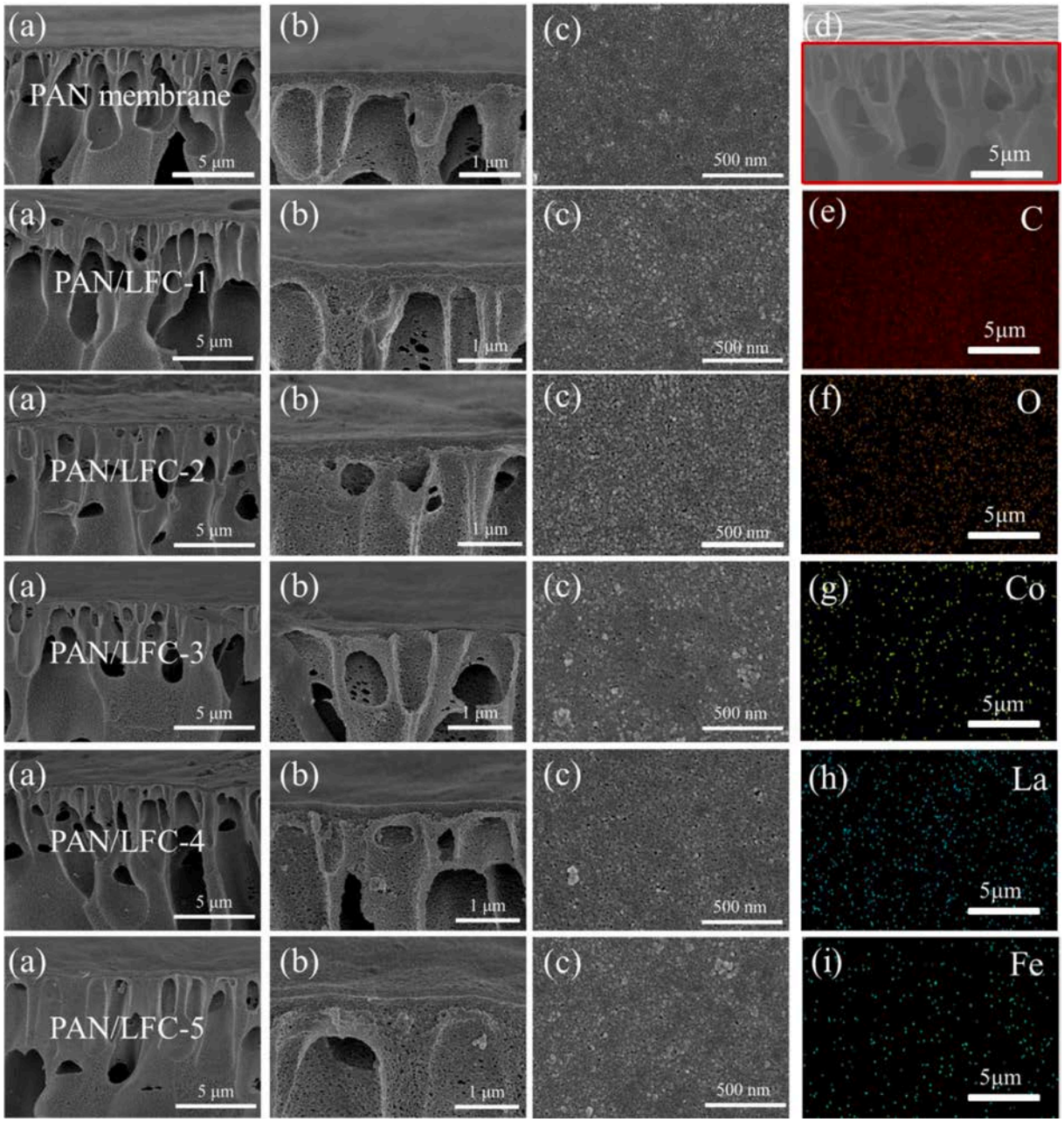

Fig. 3. SEM images of the catalytic membrane with various LFC contents. Cross-sectional structure (a), enlarged cross-section morphology (b), surface morphology (c), and EDS mapping of the catalytic membrane (d-i).

solution, which sequentially reduces the porosity of the membrane. The surface morphologies of the membranes are shown in Fig. 3(c), more pores were observed on the dense surface of the membrane as the LFC contents increased to 4%, which was beneficial to enhance the permeability of the catalytic membrane. The pore diameter was about 10 nm, which presented the pores of the ultrafiltration membrane. The distribution of LFC in membrane matrix is depicted in Fig. 3(d-i), LFC was uniformly anchored in the surface and interior channels of the membrane, enabling effective catalytic degradation of target pollutants attained by the membrane. The metal element composition of the LFC in PAN/LFC-4 membrane is listed in Table S2, and the results demonstrated that LFC was successfully embedded in the membrane matrix.

3.2. Structure and permeability of the catalytic membrane

The flux of the catalytic membrane containing ranges of LFC contents was evaluated to demonstrate the permeability for wastewater decontamination. As illustrated in Fig. 4(a), an upward trend was observed as the LFC contents augmenting, and reached the maximum of 1986.1 L/m^2h when inlaying 4% of LFC. With further increase in LFC contents, the flux started to decline, which could be caused by the diminution of both pore size and porosity of the membrane. Besides, embedding LFC in membrane structure performed an increasing trend on its porosity (about 59% when 4% LFC was introduced). Furthermore, with the integration of LFC, the hydrophilicity of membrane increased concurrently. The pristine PAN membrane possessed a WCA of 74.4°; however, with more LFC constructed in the membrane cavities, the WCA declined to 59.7°, showing better flexibility for the rapid pass-through of the penetrating fluid (Fig. 4(b)). As a prominent indicator for evaluating membrane performance, HA was used as the target pollutant to investigate the rejection capacity of the catalytic membrane. As described in Fig. 4(b), all catalytic membranes exhibited an desired HA rejection

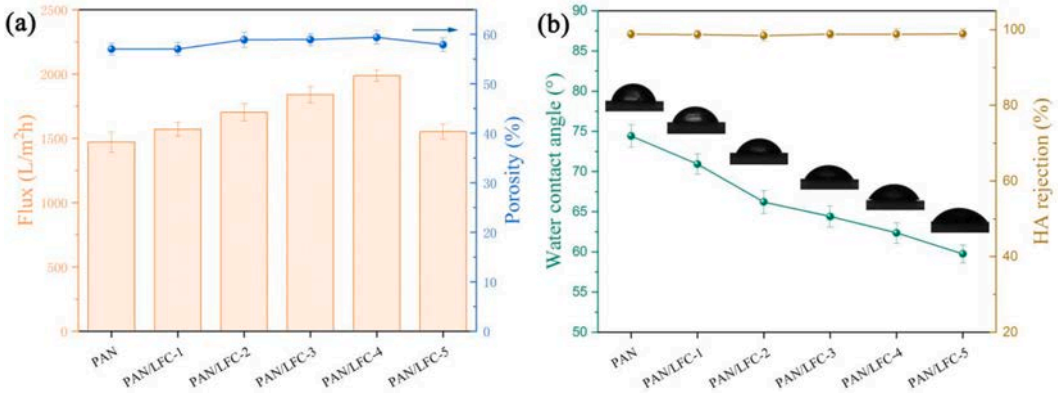

Fig. 4. Permeability of the membranes. Pure water flux and porosity (a), water contact angle and HA rejection performance (b).

ability, In other words, NOM with prominent inhibitory effect on the catalytic oxidation can be excluded by catalytic membrane, and correspondingly, the catalytic degradation occurred in membrane channels was less restricted, which further highlights the superiority of catalytic membrane for wastewater treatment.

3.3. Catalytic performance evolution of the membrane

Due to the efficient combination of the functional catalysts and membrane matrix, the catalytic membrane exhibited a satisfied elimination capacity to the target pollutant TC by activating PMS. The catalytic performance was evaluated in a cross-flow apparatus. The feed stream containing pollutants and PMS was circulated through the membrane by regulating the operating pressure. The sample passing through the membrane was withdrawn for the concentration measurement and will not be recycled into the circulation system. Firstly, the effect of LFC dosage was investigated and shown in Fig. 5(a). With the impedance by the pore size of the UF membrane, TC can pass through the membrane with feed stream; however, owing to the porous structure of the polymeric membrane, about 12.1% of TC was adsorbed during the process. It is worth noting that the pristine PAN membrane exhibited a 60% TC removal efficiency in the PMS alone, which was mainly attributed to the adsorption and an increased reaction efficiency of PMS and pollutants in the membrane channels. In other words, under the

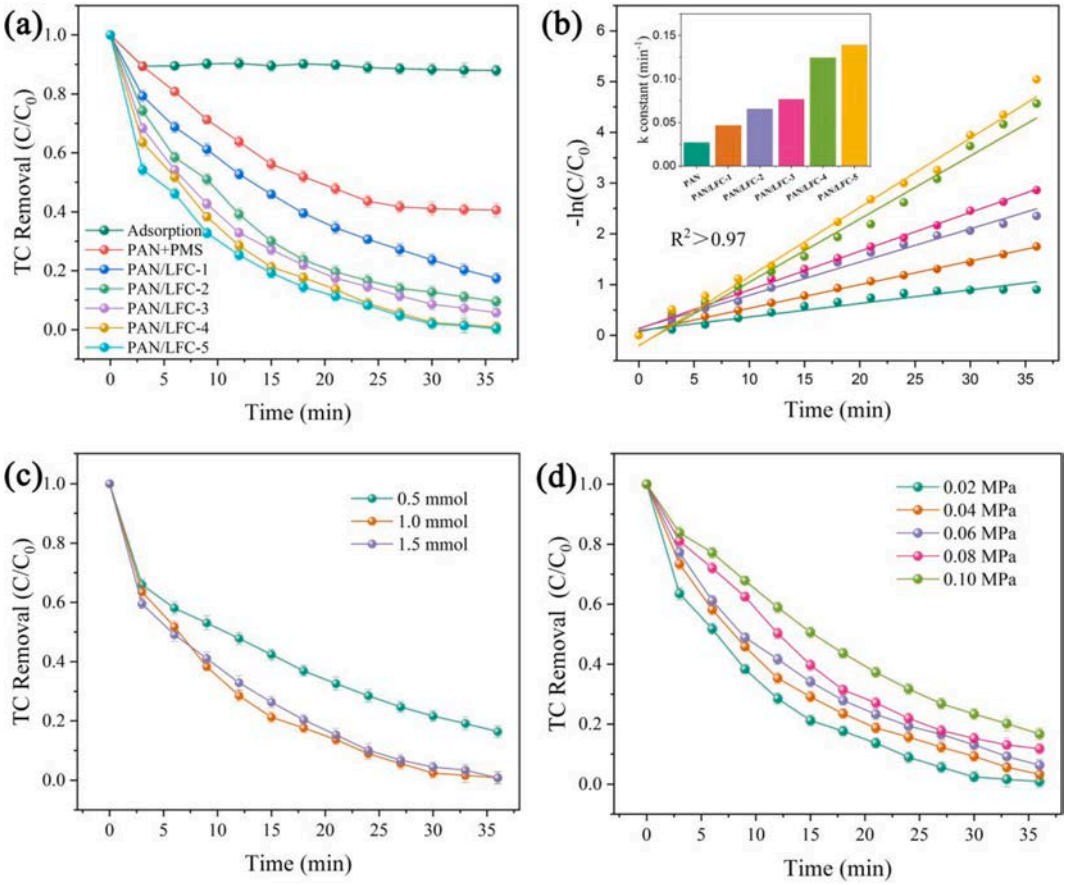

Fig. 5. TC degradation performance of the catalytic membranes. Catalytic performance of membranes containing various LFC contents (a), k constant analysis (b), effect on PMS dosage (c), and influence on operating pressure (d). Conditions: PMS = 1.0 mM; TC concentration: 10 ppm, 500 mL; effective membrane area = 7.0 cm^2 and temperature = 25 °C.

confinement of the membrane channels, the local concentration of PMS and pollutants intensified, leading to the rapid generation of ROS in membrane structure, thereby enhancing TC removal efficiency [18,40]. This phenomenon can be further confirmed when LFC was embedded into the membrane structure. Under the pressure of 0.02 MPa, the TC elimination efficiency gradually increased with the increment of LFC contents, and finally reached over 99% within 36 min when 4% LFC was incorporated. Pseudo-first-order kinetic equation was employed to analyze the reaction rate constant of the membrane. As shown in Fig. 5 (b), the k values of PAN and PAN membrane with various loading ratios of LFC was 0.0267, 0.0465, 0.0654, 0.0765, 0.1244, and 0.1392 min^{-1}, respectively, demonstrating superior catalytic degradation ability toward refractory pollutants (Effective LFC dosage is about 0.3 mg on 7.0 cm^2 for 500 mL 10 ppm TC degradation). After comprehensively considering the permeation flux and degradation performance of the catalytic membrane, PAN membrane with 4% LFC loading content was selected to investigate the catalytic performance. As depicted in Fig. 5 (c), with the addition of 0.5 mM PMS, TC removal efficiency lowered to 84.7% within 36 min. However, as PMS concentration further increased, the catalytic activity of catalytic membrane was almost unaltered. This phenomenon can be explained as followed. An excessive PMS concentration can cause self-quenching of ROS, especially in the membrane channels where the local concentration can be increased under enhanced mass transfer [15]. Therefore, 1.0 mM PMS was considered to be the appropriate amount of PMS concentration. For the catalytic membrane device, the operating pressure determines the permeation flux of membrane and then affects the retention time of pollutants in the membrane matrix. Fig. 5(d) describes the effect of operating pressure on the membrane's degradation capacity. The permeation flux and retention time of the catalytic membrane are depicted in Table S3 under various operating pressures. The TC removal efficiency decreased gradually as operating pressure elevated. In other words, a lower operating pressure is more conducive to the pollutants degradation, which also enables the operation of the catalytic membrane more cost-effective.

Fig. 6(a) depicts the influence of initial pH value on the TC degradation performance. The catalytic membrane exhibited favorable TC degradation capacity at neutral and weak alkaline conditions. However, the rapid degradation of TC at alkaline conditions may be due to the unsatisfied stability of TC itself at pH = 9. The TC degradation efficiency weakened at acidic conditions due to the slightly inhibitory effect of H^+ on $SO_4^{\cdot-}$ [43]. As shown in Fig. 6(b), increasing the concentration of pollutants is not able to improve the catalytic degradation process. Moreover, the influence of reaction temperature on the TC degradation was investigated. As illustrated in Fig. 6(c), the elevated reaction temperature significantly improves the degradation ability of the catalytic membrane. Over 99% of TC can be degraded within 33, 21, and 15 min, and k constant was 0.1244, 0.1728, and 0.2491 min^{-1} at 25, 35, and 45 °C, respectively. The augmentation of reaction temperature can not only improve the PMS activation efficiency but also reduce the reaction barrier, thus synergistically leading to the rapid decomposition of pollutants. The reaction activation energy (E_a) of catalytic membrane was analyzed based on the Arrhenius equation (Lnk = -Ea/RT + LnA). The E_a was determined to be 27.3 kJ/mol (Fig. 6(d)) and is higher than the diffusion-controlled reactions (10–13 kJ/mol) [30]. Hence, TC degradation process is mainly dominated by the catalytic degradation in membrane channels. In addition, the lower activation energy also features considerable catalytic degradation ability of catalytic membrane for the elimination of organic pollutants. The thickness of membrane significantly affects the catalytic performance, and they were controlled by adjusting the distance between casting solution and blade. As manifested in Fig. 6(e), TC removal efficiency enhanced with the increment of membrane thickness. This phenomenon can be ascribed to the following reasons: 1) more catalyst was dispersed in the membrane matrix, and simultaneously enhanced the adsorption capacity; 2) the permeation flux declined when increasing membrane thickness. As a result, the retention time of pollutants in membrane channels prolonged, causing more generation of ROS. In most of the previous work, the performance of catalytic membrane was split into two parts to demonstrate its separation and catalytic activity individually. Therefore, simulated wastewater containing HA and TC was employed to investigate the performance of catalytic membrane. Fig. 6(f) elucidated the TC removal efficiency under various amounts of HA. Notably, HA as a natural organic matter can significantly restrict the generation of ROS. However, by virtue of the membrane separation, the HA was rejected by size sieving, while TC was degraded in membrane channels.

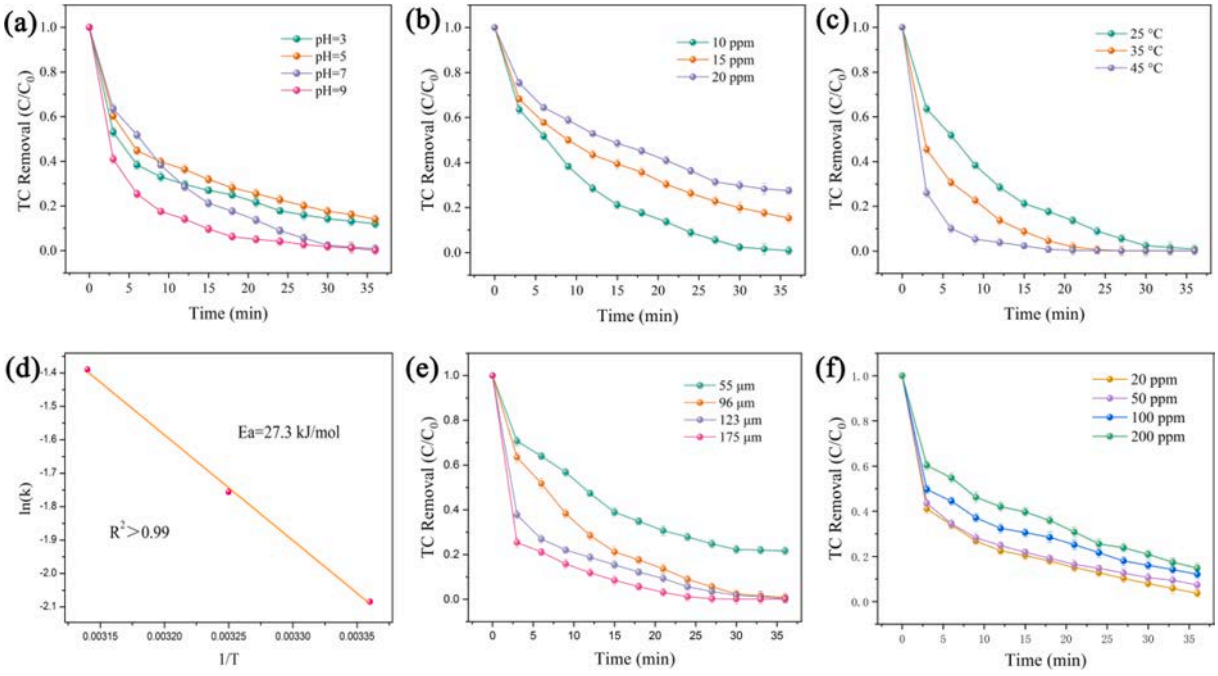

Fig. 6. Effects on various operating conditions. pH (a), TC concentration (b), temperature (c), Arrhenius equation (d), membrane thickness (e) and HA concentration (f). Conditions: PMS = 1.0 mM; TC concentration: 10 ppm, 500 mL; effective membrane area = 7.0 cm^2 and temperature = 25 °C.

Correspondingly, the catalytic membrane also possessed favorable catalytic activity in the presence of HA with concentrations ranging from 20 to 200 ppm. After 36 min of operation, over 85.2% of TC could be degraded in the presence of 200 ppm HA. In summary, the catalytic membrane that combines separation with catalysis shows better flexibility and adaptability in the field of wastewater treatment. The mineralization rate of the TC solution was validated by TOC analysis (Fig. S7). About 53.2% of TC was decomposed to CO_2 and H_2O after 3 consecutive operation processes, demonstrating satisfactory catalytic degradation ability toward organic pollutants.

With the assistance of the introduced catalytic degradation, the contaminants attached to the membrane surface and channels can be eliminated by reacting with ROS. Therefore, membrane fouling was alleviated after backwashing in the presence of PMS aqueous solution. Simulated wastewater containing 100 mg/L HA and 10 mg/L TC was employed as target pollutants, and the anti-fouling performance is depicted in Fig. S8. The pristine PAN membrane exhibited 33.4% flux recovery after three successive pollution-cleaning processes, while PAN membrane with 4% LFC exhibited a 52.4% recovery rate. Therefore, the catalytic membrane with attractive catalytic degradation capacity can better relieve membrane fouling, thus increasing the lifespan of the membrane.

3.4. Mechanism analysis

The identification of ROS was performed by radical quenching test since radical and non-radical pathways were comprehensively researched by pervious study during the activation of PMS. Scavengers of TBA and MeOH were applied to prohibit the generation of ·OH and $SO_4^{\cdot-}$, respectively [5]. As illustrated in Fig. 7(a), the excessive addition of TBA only resulted in less reduction in catalytic activity, and still 98.2% of TC can be degraded within 36 min. The introduction of MeOH triggered an obviously decline in TC degradation efficiency (64.4% in 36 min). The related results indicated that compared with ·OH, $SO_4^{\cdot-}$ played a dominant role in the radical-based catalytic degradation process. Besides, FFA was conducted to quench $^1O_2$ generated in catalytic degradation to investigate the effect of non-radical pathways on TC degradation process [41]. In the presence of 4 mM FFA, TC removal efficiency dropped by 26.6%, suggesting the participation of $^1O_2$ in the catalytic degradation process. To further prove the existence of radical and non-radical pathways in TC degradation process, EPR analysis was performed using DMPO and TEMP as trapping agents to demonstrate the generation of $SO_4^{\cdot-}$,·OH and $^1O_2$, the most symbolic ROS in TC degradation process. As presented in Fig. 7(b, c), signals of DMPO-OH (αH = αN = 14.8 G) and DMPO-SO_4 (αH = 0.78 G, αH = 14.8 G, αH = 9.6 G, and αN = 13.2 G) can be observed with relative intensities of 1:2:2:1 in PMS/catalytic membrane system, implying considerable amount of $SO_4^{\cdot-}$ and ·OH were generated by activating PMS, which ensure the occurrence of the radical-based catalytic process of TC degradation [28]. The triplet adduct of TEMP-O_2 with 1:1:1 characteristic peaks was also detected, which confirms the generation of $^1O_2$ (Fig. 7(c)). Therefore, under the synergistic effect of radicals and non-radicals, pollutants can be eliminated in the membrane channels, enabling superior catalytic degradation capacity to achieve self-cleaning properties, which further broaden the application of membrane technology. Furthermore, the durability of the catalytic membrane was evaluated. The catalytic membrane was proved to possess a favorable stability in TC degradation process through recycling test (Fig. 7(d)). Over 97.9% of TC can be degraded after five continuous cycles, which was superior to most catalysts/PMS system. The stability of the catalyst and catalytic membrane was analyzed by measuring the element valence change and corresponding metal ion leaching after catalytic degradation process. As illustrated in Fig. S9(a) and Fig. S11, the valence state of cobalt changed slightly, the corresponding proportion of Co^{II}/Co^{III} reduced from 1.04 to 0.95, while that of Fe^{II}/Fe^{III} declined from 1.21 to 0.91, indicating that Co^{II}/Co^{III} and Fe^{II}/Fe^{III} redox cycles participated in catalytic oxidation process [28]. Besides, O 1 s spectrum shown in Fig. S9(b) mainly included the decrease of highly oxidative oxygen species (O_2^{2-}/O^-)

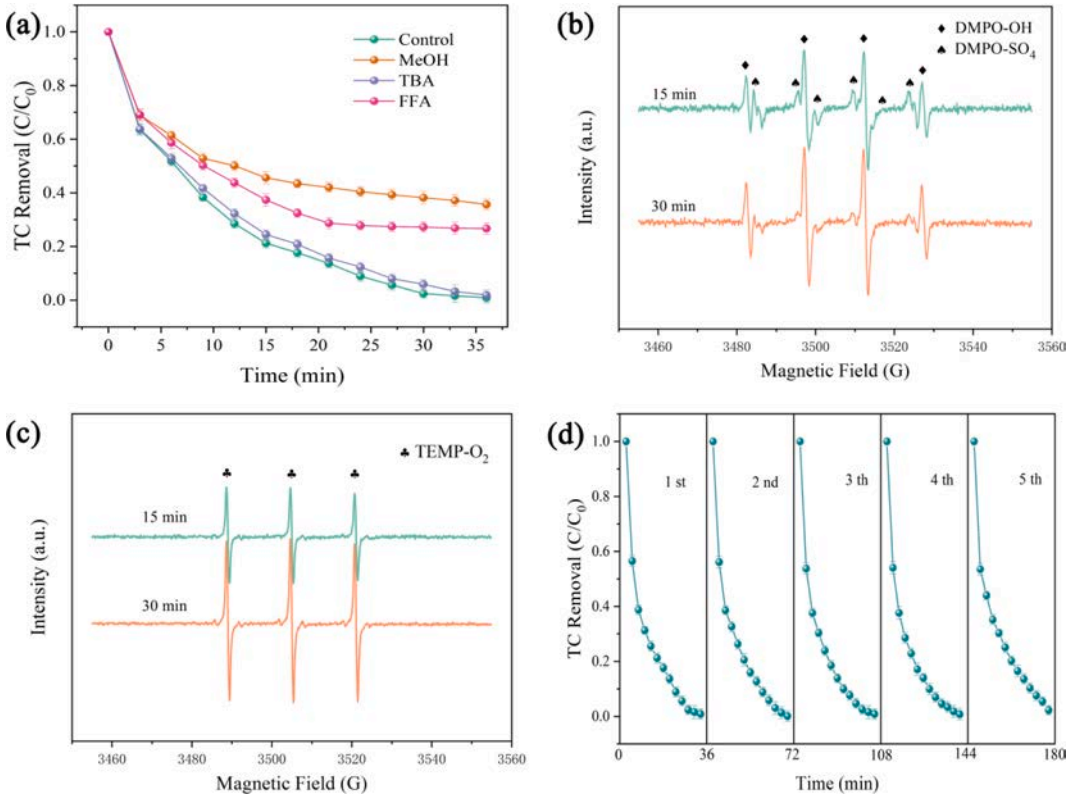

Fig. 7. Radical quenching test (a), EPR analysis of $SO_4^{\cdot-}$ and ·OH (b), EPR analysis of $^1O_2$ (c), and stability of catalytic membrane (d).

(10.9% to 5.8%) and the increase of hydroxyl groups (–OH) (42.2% to 54.7%). The lessening of O_2^{2-}/O^- demonstrates oxygen vacancies could participate in catalytic oxidation as a reaction site for singlet oxygen generation while the increase of hydroxyl groups (–OH) might due to the adsorption of the intermediate during the reaction [43]. Furthermore, as presented in Fig. S10, the structure of the catalytic membrane remained almost unchanged after reaction, which was still dominated by finger-like pores in the cross-sectional structure. The corresponded metal leaching under various operating conditions are listed in Table S4-S5, and the results demonstrated that the catalytic membrane exhibited favorable stability during cycling test, and the leaching of La, Fe, and Co elements was 0.0112, 0.0008, and 0.0132 mg/L in the fifth cycle, respectively. Besides, the catalytic membrane also possesses attractive stability under different pH conditions, and the cobalt leaching is much lower than the limitation of China (GB-25467–2010, $\leq$1 mg/L), indicating environmental-friendly characters of the catalytic membrane. The exceptional stability of catalytic membrane can be attributed to the individual operating pressure-induced membrane system. The continuous outflow of the intermediate products restricts contact time between catalysts and pollutants; however, the degradation efficiency is significantly boosted under enriched concentration gradient in membrane tortuous channels, which guarantees the stability of catalytic membrane. In summary, the catalytic membrane with exceptional stability may outperform broader application prospects than heterogeneous catalysis process.

$$Co(II) + HSO_5^- \rightarrow SO_4^{\cdot-} + OH^- + Co(III) \quad (5)$$

$$Co(III) + HSO_5^- \rightarrow SO_5^{\cdot-} + Co(II) + H^+ \quad (6)$$

$$Fe(II) + HSO_5^- \rightarrow SO_4^{\cdot-} + Fe(III) + OH^- \quad (7)$$

$$Fe(III) + HSO_5^- \rightarrow SO_5^{\cdot-} + Fe(II) + H^+ \quad (8)$$

$$SO_4^{\cdot-} + OH^- \rightarrow SO_4^{2-} + \hat{A}\cdot OH \quad (9)$$

$$Fe^{II} + Co^{III} \rightarrow Fe^{III} + Co^{II} \quad (10)$$

$$V_{\ddot{O}} \rightarrow O_o^x \quad (11)$$

$$O_o^x + HSO_5^- \rightarrow {}^1O_2 + HSO_4^- \quad (12)$$

$$SO_5^{2-} + HSO_5^- \rightarrow {}^1O_2 + SO_4^{2-} + HSO_4^- \quad (13)$$

$$TC + OH/SO_4^{\cdot-}/{}^1O_2 \rightarrow Intermediates \rightarrow CO_2 + H_2O \quad (14)$$

The underlying mechanism of the PMS activation through the catalytic membrane is proposed as Eq. (5–14). Firstly, the Co^{II}/Co^{III} redox cycle was accomplished when reacting with PMS through Eq. (5–6), during which $SO_4^{\cdot-}$ were generated [15]. However, $SO_5^{\cdot-}$ with unsatisfied redox ability were also generated through Eq. (6), which was often regarded as the rate-limited reaction step during the catalytic oxidation process, resulting in a decreased Co^{II}/Co^{III} ratio from 1.04 to 0.95 (Fig. S9(a)). On account of the introduction of Fe on B sites of perovskite, same reaction can be performed through Eq. (7–8), and the corresponded Fe^{II}/Fe^{III} dropped from 1.21 to 0.90 as illustrated in Fig. S11 [28]. Besides, ·OH can be generated as the reaction product of OH^- and $SO_4^{\cdot-}$ through Eq. (9), thereby achieving the radical-based degradation process. Furthermore, owing to the difference between the standard reduction potential of Co^{III}/Co^{II} (1.81 V) and Fe^{III}/Fe^{II} (0.77 V), the electron transfer between cobalt and iron ions with different valences was thermodynamically favorable (Eq. (10)) [34], which can also be reflected from the more obvious change of Fe valence state (Fe(II) decreased from 54.7% to 47.4%) compared with that of Co(II) (50.9% to 48.7%). In this regard, the Co ions with lower valence state were generated through electron transfer between Fe and Co component, which alleviates the restrictions of the rate-limited reaction, and then accelerates the massive generation of radicals [30,42]. Furthermore, more oxygen vacancies were generated through Fe doping (Fig. 2(c)), and the dissolved oxygen was transferred to highly oxidative oxygen species O_x^o on vacancies and then react with PMS to verify the generation of $^1O_2$ (Eq.(12)) [43,44]. In addition, the non-radical pathways can be achieved through Eq. (13) [43]. Finally, TC can be eliminated with the assistance of ·OH, $SO_4^{\cdot-}$, and $^1O_2$ through a series of catalysis reactions and then decomposed to CO_2 and H_2O for ensuring the decontamination of the organic pollutants [11,23]. Based on the above-mentioned analysis, the mechanism of the catalytic membrane is described in Fig. 8. Through the cooperation of membrane filtration and catalytic oxidation, the purification capacity of the catalytic membrane can be strengthened.

To better explore the degradation pathways of TC, the intermediate products during oxidation process were analyzed by LC/MS, and the detected compounds are shown in Fig. S12-S13. As presented in Fig. S12, the TC degradation process mainly comprised hydroxylation, demethylation, and cleavage of the functional groups, following by further ring-opening reactions [1,15]. Firstly, the intermediate with *m/z* of 427 was generated through dehydration process. Besides, hydroxylation was accomplished to the formation of the intermediate of *m/z* of 460. Secondly, dealkylation dominated the next reaction and resulted in the generation of intermediate of *m/z* of 373.1. The intermediates were further occurred with the C-N bond cleavage and ring-opening reaction, leading to the formation of the intermediates (*m/z* = 290 and 206). Furthermore, the intermediates with *m/z* of 176.9 and 149.1 were formed through hydroxylation and carboxylation processes and were oxidized to the product with *m/z* of 122.9. Finally, the intermediates can be further oxidized to CO_2 and H_2O to accomplish the mineralization process [1].

To clarify the impact of the TC and its degradation intermediates on the environment, toxicity assessment was carried out via the Toxicity Estimation Software Tool (TEST). Quantitative structure–activity relationship (QSAR) method was applied to illustrate the toxicity via the assessment of developmental toxicity, mutagenicity, daphnia magna LC50, and oral rat LD50 [45,46]. Fig. 9(a) depicts that the developmental toxicity of the intermediates, only P1 exhibited more toxicant than TC while other intermediates possessed reduced developmental toxicity. Besides, intermediate P6 was a non-toxicant. For the mutagenicity of the intermediates shown in Fig. 9(b), TC was mutagenicity positive, after the degradation process, the mutagenicity of the intermediates declined and P4, P6, P7, and P8 were mutagenicity negative. The daphnia magna LC50 of the products is illustrated in Fig. 9(c), the results demonstrated that the toxicity of the intermediates apparently weakened from very toxic to less toxic and even not harmful after catalytic membrane treatment. A similar trend was also reflected on the oral rat LD50 depicted in Fig. 9(d), as the catalytic oxidation proceed, the toxicity of oral rat LD50 was alleviated from toxic to harmful. In conclusion, the biological toxicity of TC is greatly attenuated after the catalytic membrane-induced degradation process, which highlights the feasibility and application prospects of the catalytic membrane. The performance comparisons of the catalytic membranes are summarized in Table S6. Correspondingly, PAN/LFC membrane features desirable separation and degradation performance compared to other catalytic membranes, which is relating to the integration of perovskite-based catalyst, which not only optimizes the hydrophilicity of the membrane but also endows sufficient reaction sites in the membrane channels. Therefore, the wastewater remediation efficiency can be further enhanced through the combination of membrane technology and catalytic oxidation.

4. Conclusion

In this work, the catalytic membrane was facilely prepared by embedding the functional catalysts on membrane channels. With the integration of membrane filtration and PMS-induced catalytic oxidation,

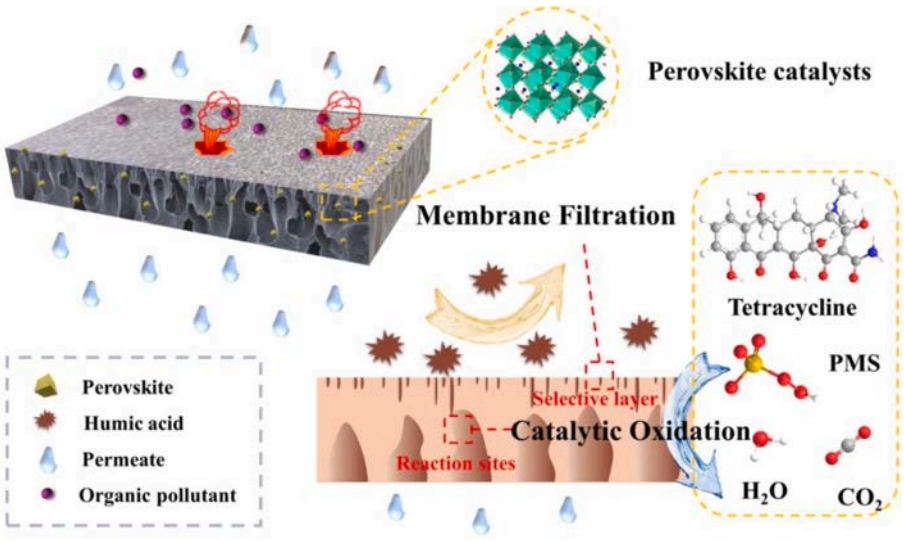

Fig. 8. Mechanism diagram of the catalytic membrane.

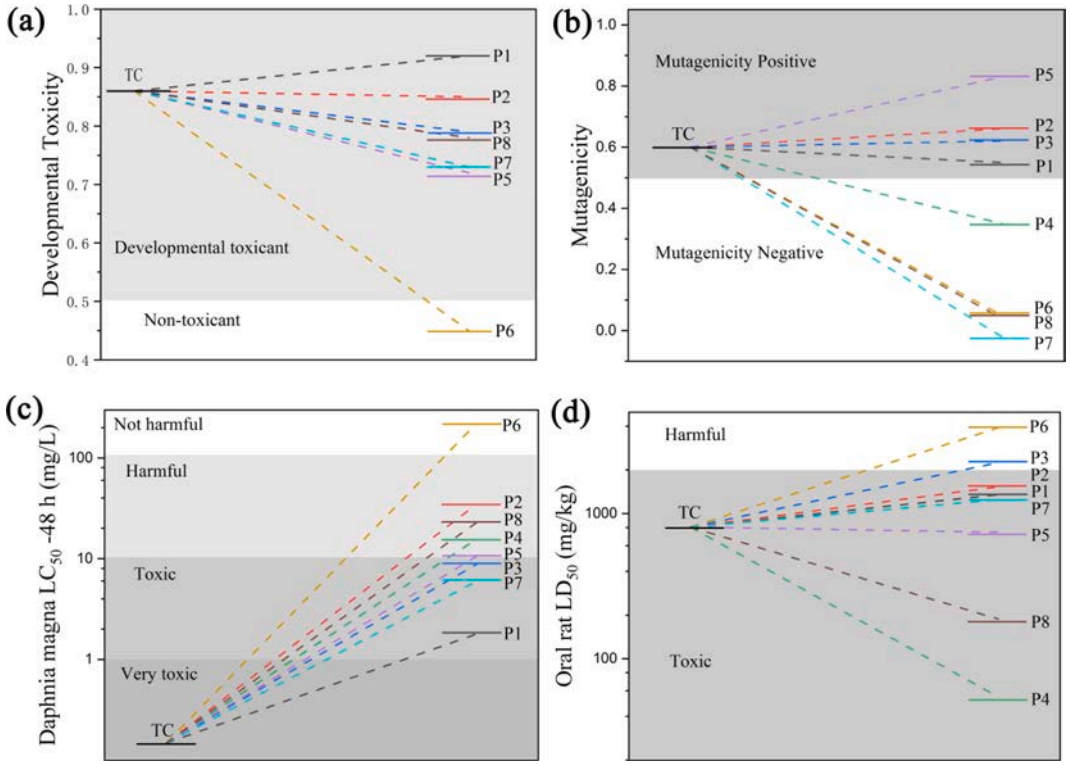

Fig. 9. Toxicity analysis of TC and degraded intermediates. Developmental toxicity (a), mutagenicity (b), daphnia magna LC_{50} (c), and oral rat LD_{50} (d).

the catalytic membrane fulfilled favorable catalytic performance toward TC degradation together with superior HA rejection capacity under low operating pressures, which outperformed previous catalytic membranes. The massive generation of radical $SO_4^{\cdot-}$ and $^1O_2$ in membrane channels was proved, which was responsible for the rapid degradation of pollutants and the favorable self-cleaning capacity. Besides, the catalytic membrane also demonstrated superior stability based on the continuous outflow of intermediate products and the restricted contact time. Furthermore, the attenuated biological toxicity of the treated wastewater was investigated, further highlighting versatile prospects of wastewater remediation.

Declaration of Competing Interest

The authors declare that they have no known competing financial interests or personal relationships that could have appeared to influence the work reported in this paper.

Acknowledgments

The authors greatly acknowledge the financial support of National Natural Science Foundation of China (22078233).

Appendix A. Supplementary data

Supplementary data to this article can be found online at https://doi.org/10.1016/j.cej.2022.135163.

References

[1] Q. Wu, H. Yang, L. Kang, Z. Gao, F. Ren, Fe-based metal-organic frameworks as Fenton-like catalysts for highly efficient degradation of tetracycline hydrochloride over a wide pH range: acceleration of Fe(II)/Fe(III) cycle under visible light irradiation, Appl. Catal. B 263 (2020), 118282.

[2] J. Li, L. Zhao, R. Zhang, H.H. Teng, L.P. Padhye, P. Sun, Transformation of tetracycline antibiotics with goethite: Mechanism, kinetic modeling and toxicity evaluation, Water Res. 199 (2021), 117196.

[3] F. Ghanbari, M. Moradi, Application of peroxymonosulfate and its activation methods for degradation of environmental organic pollutants: Review, Chem. Eng. J. 310 (2017) 41–62.

[4] Y. Ji, Y. Shi, L. Wang, J. Lu, Denitration and renitration processes in sulfate radical-mediated degradation of nitrobenzene, Chem. Eng. J. 315 (2017) 591–597.

[5] W.-D. Oh, Z. Dong, T.-T. Lim, Generation of sulfate radical through heterogeneous catalysis for organic contaminants removal: Current development, challenges and prospects, Appl. Catal. B 194 (2016) 169–201.

[6] S. Zhang, H. Gao, X. Xu, R. Cao, H. Yang, X. Xu, J. Li, MOF-derived CoN/N-C@SiO_2 yolk-shell nanoreactor with dual active sites for highly efficient catalytic advanced oxidation processes, Chem. Eng. J. 381 (2020), 122670.

[7] L. Wu, B. Li, Y. Li, X. Fan, F. Zhang, G. Zhang, Q. Xia, W. Peng, Preferential Growth of the Cobalt (200) Facet in Co@N–C for Enhanced Performance in a Fenton-like Reaction, ACS Catal. 11 (2021) 5532–5543.

[8] H. Xia, Z. Zhang, J. Liu, Y. Deng, D. Zhang, P. Du, S. Zhang, X. Lu, Novel Fe-Mn-O nanosheets/wood carbon hybrid with tunable surface properties as a superior catalyst for Fenton-like oxidation, Appl. Catal. B 259 (2019), 118058.

[9] Y. Park, C. Kim, M. Kim, S. Kim, W. Choi, Ambient-Temperature Catalytic Degradation of Aromatic Compounds on Iron Oxide Nanorods Supported on Carbon Nanofiber Sheet, Appl. Catal. B 259 (2019) 118066, https://doi.org/10.1016/j.apcatb.2019.118066.

[10] T. Zeng, X. Zhang, S. Wang, H. Niu, Y. Cai, Spatial confinement of a Co_3O_4 catalyst in hollow metal-organic frameworks as a nanoreactor for improved degradation of organic pollutants, Environ. Sci. Technol. 49 (2015) 2350–2357.

[11] X. Li, X. Yan, X. Hu, R. Feng, M. Zhou, L. Wang, Hollow Cu-Co/N-doped carbon spheres derived from ZIFs as an efficient catalyst for peroxymonosulfate activation, Chem. Eng. J. 397 (2020), 125533.

[12] Y. Zhao, D. Wu, Y. Chen, Y. Li, X. Fan, F. Zhang, G. Zhang, W. Peng, Thermal removal of partial nitrogen atoms in N-doped graphene for enhanced catalytic oxidation, J. Colloid Interface Sci. 585 (2021) 640–648.

[13] T. Ma, L. Liu, B. Meng, J. Gao, S. Wang, S. Liu, Heterogeneous activation of peroxymonosulfate via a Ag-$La_{0.8}Ca_{0.2}Fe_{0.94}O_{3-\delta}$ perovskite hollow fibre membrane reactor for dye degradation, Sep. Purif. Technol. 211 (2019) 298–302.

[14] Y.n. Liu, R. Qu, X. Li, Y. Wei, L. Feng, A bifunctional β-MnO_2 mesh for expeditious and ambient degradation of dyes in activation of peroxymonosulfate (PMS) and simultaneous oil removal from water, Journal of colloid and interface science, 579 (2020) 412-424.

[15] L. Zhang, Y. Zhang, J. Wei, W. Liu, Perovskite $LaFe_xCo_{1-x}O_{3-\lambda}$ deposited SiO_2 catalytic membrane for deeply cleaning wastewater, Chem. Eng. J. 403 (2021), 126386.

[16] H. Shan, X. Dong, X. Cheng, Y. Si, J. Yu, B. Ding, Highly flexible, mesoporous structured, and metallic Cu-doped C/SiO_2 nanofibrous membranes for efficient catalytic oxidative elimination of antibiotic pollutants, Nanoscale 11 (2019) 14844–14856.

[17] N. Li, X. Lu, M. He, X. Duan, B. Yan, G. Chen, S. Wang, Catalytic membrane-based oxidation-filtration systems for organic wastewater purification: A review, J. Hazard. Mater. 414 (2021) 125478, https://doi.org/10.1016/j.jhazmat.2021.125478.

[18] H. Lin, Q. Fang, W. Wang, G. Li, J. Guan, Y. Shen, J. Ye, F. Liu, Prussian blue/PVDF catalytic membrane with exceptional and stable Fenton oxidation performance for organic pollutants removal, Appl. Catal. B 273 (2020), 119047.

[19] Z. He, S. Mahmud, S. Zhao, Y. Yang, L. Zhu, Y. Zhao, Q. Zeng, Z. Xiong, C. Hu, Hierarchically Active Poly(vinylidene fluoride) Membrane Fabricated by In Situ Generated Zero-Valent Iron for Fouling Reduction, ACS Appl. Mater. Interfaces 12 (2020) 10993–11004.

[20] S. Zheng, H. Chen, X. Tong, Z. Wang, J.C. Crittenden, M. Huang, Integration of a Photo-Fenton Reaction and a Membrane Filtration using CS/PAN@FeOOH/g-C_3N_4 Electrospun Nanofibers: Synthesis, Characterization, Self-cleaning Performance and Mechanism, Applied Catalysis B: Environmental 281 (2021), 119519.

[21] L. Zhang, N.a. Yang, Y. Han, X. Wang, L. Zhang, Y. Sun, B. Jiang, Highly dispersed β-FeOOH nanocatalysts anchored in confined membrane pores for simultaneously improving catalytic and separation performance, Sep. Purif. Technol. 279 (2021) 119684, https://doi.org/10.1016/j.seppur.2021.119684.

[22] Y. Bao, Y.S. Tay, T.-T. Lim, R. Wang, R.D. Webster, X. Hu, Polyacrylonitrile (PAN)-induced carbon membrane with in-situ encapsulated cobalt crystal for hybrid peroxymonosulfate oxidation-filtration process: Preparation, characterization and performance evaluation, Chem. Eng. J. 373 (2019) 425–436.

[23] S. Wang, J. Tian, Q. Wang, F. Xiao, S. Gao, W. Shi, F. Cui, Development of CuO coated ceramic hollow fiber membrane for peroxymonosulfate activation: a highly efficient singlet oxygen-dominated oxidation process for bisphenol a degradation, Appl. Catal. B 256 (2019), 117783.

[24] Y. Zhao, D. Lu, C. Xu, J. Zhong, M. Chen, S. Xu, Y. Cao, Q. Zhao, M. Yang, J. Ma, Synergistic oxidation-filtration process analysis of catalytic $CuFe_2O_4$-Tailored ceramic membrane filtration via peroxymonosulfate activation for humic acid treatment, Water Res. 171 (2020), 115387.

[25] S. Zhang, T. Hedtke, Q. Zhu, M. Sun, S. Weon, Y. Zhao, E. Stavitski, M. Elimelech, J.-H. Kim, Membrane-Confined Iron Oxychloride Nanocatalysts for Highly Efficient Heterogeneous Fenton Water Treatment, Environ. Sci. Technol. 55 (2021) 9266–9275.

[26] H. Zhang, X. Wang, Y. Li, K. Zuo, C. Lyu, A novel MnOOH coated nylon membrane for efficient removal of 2,4-dichlorophenol through peroxymonosulfate activation, J. Hazard. Mater. 414 (2021), 125526.

[27] M. Wang, Y. Cui, H. Cao, P. Wei, C. Chen, X. Li, J. Xu, G. Sheng, Activating peroxydisulfate with Co_3O_4/$NiCo_2O_4$ double-shelled nanocages to selectively degrade bisphenol A – A nonradical oxidation process, Appl. Catal. B 282 (2021), 119585.

[28] J. Wei, D. Han, J. Bi, J. Gong, Fe-doped ilmenite $CoTiO_3$ for antibiotic removal: Electronic modulation and enhanced activation of peroxymonosulfate, Chem. Eng. J. 423 (2021), 130165.

[29] J. Zhu, H. Li, L. Zhong, P. Xiao, X. Xu, X. Yang, Z. Zhao, J. Li, Perovskite Oxides: Preparation, Characterizations, and Applications in Heterogeneous Catalysis, ACS Catal. 4 (2014) 2917–2940.

[30] L. Zhang, L. Zhang, Y. Sun, B. Jiang, Porous ZrO_2 encapsulated perovskite composite oxide for organic pollutants removal: Enhanced catalytic efficiency and suppressed metal leaching, J. Colloid Interface Sci. 596 (2021) 455–467.

[31] Q. Pan, Q. Gao, G. Gao, M. Liu, B. Han, K. Xia, C. Zhou, Composition-engineered $LaCoO_3$-based monolithic catalysts for easily operational and robust peroxymonosulfate activation, Chem. Eng. J. 424 (2021), 130574.

[32] S. Royer, D. Duprez, F. Can, X. Courtois, C. Batiot-Dupeyrat, S. Laassiri, H. Alamdari, Perovskites as substitutes of noble metals for heterogeneous catalysis: dream or reality, Chem. Rev. 114 (2014) 10292–10368.

[33] S. Lu, G. Wang, S. Chen, H. Yu, F. Ye, X. Quan, Heterogeneous activation of peroxymonosulfate by $LaCo_{1-x}Cu_xO_3$ perovskites for degradation of organic pollutants, J. Hazard. Mater. 353 (2018) 401–409.

[34] J. Wei, J. Bi, L. Zhang, D. Han, J. Gong, Gravity-driven Fe-doped $CoTiO_3$/SiO_2 fiber membrane with open catalytic network: Activation of peroxymonosulfate and efficient pollutants removal, Sep. Purif. Technol. 280 (2022) 119975, https://doi.org/10.1016/j.seppur.2021.119975.

[35] X. Pang, Y. Guo, Y. Zhang, B. Xu, F. Qi, $LaCoO_3$ perovskite oxide activation of peroxymonosulfate for aqueous 2-phenyl-5-sulfobenzimidazole degradation: Effect of synthetic method and the reaction mechanism, Chem. Eng. J. 304 (2016) 897–907.

[36] X. Luo, L. Bai, J. Xing, X. Zhu, D. Xu, B. Xie, Z. Gan, G. Li, H. Liang, Ordered Mesoporous Cobalt Containing Perovskite as a High-Performance Heterogeneous Catalyst in Activation of Peroxymonosulfate, ACS Appl. Mater. Interfaces 11 (2019) 35720–35728.

[37] C. Su, X. Duan, J. Miao, Y. Zhong, W. Zhou, S. Wang, Z. Shao, Mixed Conducting Perovskite Materials as Superior Catalysts for Fast Aqueous-Phase Advanced Oxidation: A Mechanistic Study, ACS Catal. 7 (1) (2017) 388–397.

[38] J. Miao, X. Duan, J. Li, J. Dai, B. Liu, S. Wang, W. Zhou, Z. Shao, Boosting performance of lanthanide magnetism perovskite for advanced oxidation through lattice doping with catalytically inert element, Chem. Eng. J. 355 (2019) 721–730.

[39] Q. Ji, L. Bi, J. Zhang, H. Cao, X.S. Zhao, The role of oxygen vacancies of ABO_3 perovskite oxides in the oxygen reduction reaction, Energy Environ. Sci. 13 (2020) 1408–1428.

[40] Y. Chen, G. Zhang, H. Liu, J. Qu, Confining Free Radicals in Close Vicinity to Contaminants Enables Ultrafast Fenton-like Processes in the Interspacing of MoS_2 Membranes, Angew. Chem. Int. Ed. 58 (2019) 8134–8138.

[41] N.a. Lu, H. Lin, G. Li, J. Wang, Q. Han, F.u. Liu, ZIF-67 derived nanofibrous catalytic membranes for ultrafast removal of antibiotics under flow-through filtration via non-radical dominated pathway, J. Membr. Sci. 639 (2021) 119782, https://doi.org/10.1016/j.memsci.2021.119782.

[42] P. Liang, D. Meng, Y.i. Liang, Z. Wang, C. Zhang, S. Wang, Z. Zhang, Cation deficiency tuned $LaCoO_{3-\delta}$ perovskite for peroxymonosulfate activation towards bisphenol A degradation, Chem. Eng. J. 409 (2021) 128196, https://doi.org/10.1016/j.cej.2020.128196.

[43] M. Zhu, J. Miao, X. Duan, D. Guan, Y. Zhong, S. Wang, W. Zhou, Z. Shao, Postsynthesis Growth of CoOOH Nanostructure on $SrCo_{0.6}Ti_{0.4}O_{3-\delta}$ Perovskite Surface for Enhanced Degradation of Aqueous Organic Contaminants, ACS Sustainable Chem. Eng. 6 (11) (2018) 15737–15748.

[44] J. Miao, J. Sunarso, X. Duan, W. Zhou, S. Wang, Z. Shao, Nanostructured Co-Mn containing perovskites for degradation of pollutants: Insight into the activity and stability, J. Hazard. Mater. 349 (2018) 177–185.

[45] X.i. Tao, P. Pan, T. Huang, L. Chen, H. Ji, J. Qi, F. Sun, W. Liu, In-situ construction of $Co(OH)_2$ nanoparticles decorated urchin-like WO_3 for highly efficient degradation of sulfachloropyridazine via peroxymonosulfate activation: Intermediates and DFT calculation, Chem. Eng. J. 395 (2020) 125186, https://doi.org/10.1016/j.cej.2020.125186.

[46] L. Chen, H. Ji, J. Qi, T. Huang, C.-C. Wang, W. Liu, Degradation of acetaminophen by activated peroxymonosulfate using $Co(OH)_2$ hollow microsphere supported titanate nanotubes: Insights into sulfate radical production pathway through CoOH$^+$ activation, Chem. Eng. J. 406 (2021), 126877.